Supplementary Information for

Molecular-Scale Structure of Electrode-Electrolyte Interfaces: The Case of Platinum in Aqueous Sulfuric Acid

Cheng Hao Wu[1,2,§], Tod A. Pascal[3,§], Artem Baskin[3], Huixin Wang[2,4], Hai-Tao Fang[2,4], Yi-Sheng Liu[5], Yi-Hsien Lu[2], Jinghua Guo[5,6], David Prendergast[3], and Miquel B. Salmeron[2,7,*]

[1] *Department of Chemistry, University of California, Berkeley, Berkeley CA, USA*

[2] *Materials Science Division, Lawrence Berkeley National Laboratory, Berkeley CA, USA*

[3] *The Molecular Foundry, Lawrence Berkeley National Laboratory, Berkeley CA, USA*

[4] *School of Materials Science and Engineering, Harbin Institute of Technology, Harbin, P. R. China*

[5] *The Advanced Light Source, Lawrence Berkeley National Laboratory, Berkeley CA, USA*

[6] *Department of Chemistry and Chemical Biology, University of California, Santa Cruz, Santa Cruz CA, USA*

[7] *Department of Materials Science and Engineering, University of California, Berkeley, Berkeley CA, USA*

§These authors contributed equally to this work

*Corresponding Email: mbsalmeron@lbl.gov

Methods

1. Materials and thin film preparation

Standard 0.1N (0.05M) sulfuric acid solution was purchased from Sigma-Aldrich and used without any purification or other treatment. The Pt (or Au) thin film (15 nm) was evaporated onto the flat side of the Si_3N_4 window by an e-beam evaporator under 10^{-8} Torr base pressure. A thin Ti layer (2 nm) was deposited prior to the Pt deposition to achieve better adhesion between Pt and Si_3N_4 membrane. The Ti adhesion layer is fully covered by platinum and no TiO_2 signature could be seen in all the O K-edge TEY-XAS spectrum acquired.

2. Experiment configurations of *operando* XAS measurements

The *operando* XAS experiments were performed at beamline 8.0.1.3 (Wet-RIXS) endstation of the Advanced Light Source, the synchrotron facility at Lawrence Berkeley National Laboratory.

As previously described[1] and illustrated in Fig. S1, the Si_3N_4 window covered with Pt or Au thin film was assembled in a flow liquid cell, containing a Pt wire and a miniature Ag/AgCl electrode as counter electrode (CE) and reference electrodes (RE), respectively. During *operando* XAS measurements, the bias was applied between the working electrode (WE), i.e. the Pt thin film or Au thin film, and the Pt CE, and the voltage was provided by the SRS570 pre-amplifier bias output function. The reported potentials with respect to the Ag/AgCl RE, were the average values of potential difference between WE and RE measured before and after the acquisition of each spectrum under x-ray illumination. At potentials above open circuit potential (OCP), the total drift in potential with respect to the RE is small (<50mV) during the data acquisition time of each spectrum (~20min). At potentials below OCP however, the drift becomes larger and the quality of the EY-XAS signal becomes noticeably worse, as illustrated in Fig. S6.

Although it is feasible to conduct three-electrode constant potential amperometry in the liquid cell using a commercial potentiostat, such configuration introduces a much higher level of noise during collection of EY signal. The two-electrode configuration introduces substantially less noise and generates reproducible data. The bias applied between WE and CE were limited within the ±1.3V window to avoid substantial water electrolysis reactions, which will produce large volume of gases leading to pressure build-up and rupture of the Si_3N_4 window.

Total fluorescence yield (TFY) XAS spectra were collected simultaneously with EY-XAS during each measurement, using a negatively biased channeltron detector. Because TFY-XAS measures the photons emitted after x-ray excitation, whose mean free path in liquids is on the order of μm, TFY-XAS is therefore a bulk-sensitive measurement in comparison with surface- or interface-sensitive EY-XAS.

3. Notes on the electrochemical measurements inside the liquid cell

We note that the cyclic voltammetry (CV) curve we collected inside the *in-situ* cell, as shown in Figure S2, is slightly tilted, particular in the double-layer region and H UPD region. Such tilting is caused, at least in part, by reduction reaction of dissolved O_2 in the H_2SO_4 solution, which is known to contribute small negative current in those two regions. In addition, the non-ideal geometry and electrode configuration inside the tiny liquid cell may also have impacts on the shape of the CV curves.

In a conventional CV measurement of Pt electrode in H_2SO_4, the solution is typically purged with Ar continuously to remove dissolved O_2. In our measurements, we did not purge Ar in the H_2SO_4 solution for the following reasons:

a. The volume of the liquid reservoir in the *in-situ* cell is very small (<1ml). All the tubing in and out of the cell also has very smaller diameter. Small cell volume and thin tubing are part of the precautions to prevent severe liquid contamination in the XAS vacuum chamber in the event of Si_3N_4 window bursting. For such small volume, it is almost impossible to implement purging or bubbling capability inside the cell.

b. Even if such capability were possible, bubbling in front of the 100nm-thick Si_3N_4 membrane substantially increases the chance of window bursting, which makes the already challenging experiments more difficult. Bubbling will also cause vigorous convection inside the solution, which induces local ion flow in random directions. Such random ionic current near the thin film WE would certainly interfere with the collection of tiny TEY current.

c. Each spectrum typically takes 20-30 min to collect. To prevent the interference of any ion flow as we discussed earlier, we stop the liquid flow during the acquisition of each spectrum. The connections that allow solution in and out of the liquid cell are not designed to be vacuum-tight and O_2 will slowly diffuse through those connections and dissolved into the solution within 30 min. Even if we use H_2SO_4 solution that is Ar-purged outside the cell, we will still have O_2 slowly dissolved into the solution during the XAS measurement.

Nevertheless, our findings in this study mostly focused in the potential range above double-layer region (> 0.6V vs RHE), where the impact of ORR side reaction is minimum. In fact, if the dissolved O_2 has any impact on the interface chemistry, it would make the oxide formation easier; but we didn't see any evidence of oxide in our XAS spectra. Therefore, we do not think the tilt of the CV in the lower bias region affects the validity of our conclusions.

We should also note that x-ray illumination of the WE induced a potential drop of ~ 0.3V relative to RE, because of the extra (secondary electron) current induced by x-ray illumination. At low current conditions (such as OCP),

the small TEY current (typically 1-10nA) will lead to re-equilibration between WE and CE and thus the shift in measured potential relative to RE. This is why our OCP potentials are approximately 0.3V more negative than the values commonly reported in the literature (0.5-0.6V vs Ag/AgCl). But when the ionic current is large (e.g. around the anodic or cathodic peaks), such small current is negligible; as a result, its impact on relative potentials is very small. Overall, we did not observe shifts or distortions in the CV profile under x-ray illumination. For the sake of consistency, all the potentials relative to RE reported in this study were recorded under x-ray illumination.

4. XAS spectra analysis

For each of the raw XAS spectrum, the intensity was first normalized by the photon flux, represented by the TEY current from a gold mesh installed upstream in the x-ray pipeline. A straight-line background was subtracted from the flux-normalized spectrum based on the linear fit of the flat region before the absorption edge. All the spectra were normalized again by setting the intensity of the flat tail (between 550 and 560 eV) to unity.

Numerical fitting was performed in some of the XAS spectra using four Gaussian components after subtraction of an arctan background. The purpose of such fitting was to quantitatively compare the width of the pre-peaks at 535 eV, without attempt to determine the exact physical origin of each component.

5. Notes on saturation effects

As pointed out in the main text, the O K-edge spectra acquired at the most positive potentials (>1V vs Ag/AgCl) exhibit long flat tails, reminiscent of bulk water XAS spectra that suffer from saturation effects. Such effect is typically seen in the fluorescence yield (FY) XAS but not in electron yield (EY) XAS, with the exception of low-energy partial electron yield (PEY), as demonstrated by Nilsson et al.[2] where secondary electrons with very low kinetic energy (<20eV) are filtered and collected via a biased electrode. Because the mean free path of these low energy electrons can be comparable to that of soft x-ray photons, such PEY XAS measurements can suffer from saturation effects.

While an increase in current due to low energy secondary electrons originating deeper in the solution and attracted to the positive electrode voltage seems plausible in principle, one should also consider the countering effect of screening of the electrode potential by the electrical double layer. Although these effects are not yet fully understood, we believe that saturation effects are not severe enough here to substantially distort the EY-XAS spectra, at least for positive bias below ~1V. Indeed, the lack of pre-edge features (related to broken hydrogen bonds) in the XAS spectra collected at OCP indicates that these low energy electrons can only account for a very small portion of the electrons collected in the EY-XAS measurements because otherwise the EY-XAS spectrum would resemble the saturated spectrum of bulk water with strong pre-peak at 535eV. One would also expect saturated bulk water spectra at positive bias no matter what solute in the aqueous solution. The fact that we obtain

different potential-dependence XAS under positive potentials for both Au-H$_2$O and Au/Pt-H$_2$SO$_4$(aq) interfaces suggests that this is not the case.

6. First Principles Molecular Dynamics (FPMD) Simulations

We used a system comprising a Pt electrode (represented by a 4×4×6 supercell of the fundamental unit cell containing 96 Pt atoms in total, with the (111) surface exposed and a surface area of 1.12×0.97 nm^2), 119 water molecules, and various amounts of H$_2$SO$_4$/HSO$_4^-$/SO$_4^{2-}$ molecules with the corresponding amount of H$_3$O$^+$ molecules to achieve overall neutrality in the system. Surface coverages ranging from 0.083 (1 sulfate species) to 0.83 (10 sulfate species) were considered.

We first equilibrated each system by performing 25ps constant volume, constant temperature (canonical or NVT ensemble) FPMD simulations at 350K within density functional theory (DFT). We employed a modified version of the mixed Gaussian and plane wave code[3] CP2K/Quickstep.[4] The electronic structure of the atoms was described using a triple-ζ basis set with two additional sets of polarization functions (TZV2P)[5] and a 320 Ry plane-wave cutoff. We used the Perdew-Burke-Ernzerhof (PBE) form of the generalized-gradient approximation of the unknown exchange-correlation potential in DFT,[6] and the Brillouin zone is sampled at the Γ-point only. Interactions between the valence electrons and the ionic cores are described by norm-conserving pseudopotentials.[7,8] The Poisson equation is solved using an efficient Wavelet-based solver.[9] We overcome the poor description of the short-range dispersive forces within the PBE-GGA exchange-correlation functional by employing the DFTD3 empirical corrections of Grimme et al.[10] Snapshots of the system were saved at every step. We recognize that particular chemical species near the interface can efficiently change identity via exchange of protons through surrounding water molecules and that there is a known overestimation of the rate of dissociation of bisulfate (HSO$_4^-$ + H$_2$O ⇔ H$_3$O$^+$ + SO$_4^{2-}$) in the bulk phase when employing the generalized-gradient approximation within DFT-based FPMD.[11] Therefore when performing FPMD simulations we impose fixed speciation by restricting the number of protons associated to each molecule through a constraint on the coordination number.

After equilibration, the binding free energy of a randomly selected sulfate molecule to the platinum electrode was separately obtained from umbrella sampling[12] calculations, employing the center of mass distances as the collective variable. In other words, we introduced a reaction coordinate ξ and defined a harmonic umbrella potential function V(ξ(r)) in the following form:

$$V\left(\xi\left(r\right)\right) = k\left(\xi\left(r\right) - r_0\right)^2$$

where k is the force constant [10 kcal/(mol Å^2)], and r_0 is the equilibrium distance. We used a simulation time step of 0.5fs. Separate simulations were run, with biased potentials centered along the reaction coordinate in 20

windows, with 0.5Å displacements from 0 to 1nm. We verified that these simulations parameters yielded overlapping Gaussian distributions at various r_0 distances. At each displacement, we carried out 5ps NVT dynamics, with the system coordinates saved every 10fs. The free energy of binding was subsequently obtained from the potential of mean force, calculated using the weighted histogram analysis method,[13,14] with a convergence tolerance of $1×10^{-4}$ kcal/mol. We ignored the first 1ps of dynamics at each window when calculating the free energy.

7. XAS spectra simulations

During the last 10ps of NVT FPMD equilibrium simulation, snapshots of the atomic positions of the system were saved every 0.5ps (a total of 20 snapshots for each system), and used as input for an in-house code employing constrained-occupancy DFT calculations within the XCH approximation[15–17] to calculate the XAS spectra. Plane-wave pseudopotential calculations using ultrasoft pseudopotentials[18] were performed using the PWSCF code within the Quantum-ESPRESSO package.[19] We used a kinetic energy cut-off for electronic wave functions of 25 Ry and a density cut-off of 200 Ry. The core-excited Kohn-Sham eigenspectrum was generated using the XCH approach.[17] Based on a numerically converged self-consistent charge density, we generated the unoccupied states for our XAS calculations non-self-consistently by sampling the first Brillouin zone at the Γ-point, employing an implementation of the Shirley interpolation scheme[20] generalized to handle ultra-soft pseudopotentials.[21] Matrix elements were evaluated within the PAW frozen-core approximation.[22] Core-excited ultrasoft pseudopotentials and corresponding atomic orbitals were generated with the Vanderbilt code.[18] Each computed transition was convoluted with a 0.2 eV Gaussian function to produce continuous spectra.

Because of the use of pseudopotentials we can only reliably compare the calculated relative excitation energies. We used an alignment scheme based on energy differences between ground and core-excited states of the system and those of an isolated atom in the same simulation cell.[16,23] Direct comparison to experiment is accomplished by first calibrating an unambiguous reference system. In the case of the oxygen compounds considered in this study, we rigidly shifted the first major peak in the oxygen K-edge XAS of an isolated CO_2 molecule by +526.9 eV to match the same in a gas phase experiment.[24] This empirical shift, is unique to the pseudopotentials employed in this study, and is applied to all subsequent calculated spectra. Previous experience has shown that this alignment scheme predicts XAS peak positions to within ~0.1 eV,[15,16] which is close to the experimental uncertainty in this energy range. It is well know that Kohn-Sham DFT within the PBE approximation underestimates band gaps[25,26] and concomitantly band-widths due to inaccurate quasiparticle (excitation) energies.[27,28] As a result, the calculated XAS spectrum is usually too narrow compared to experiments. We thus dilated the computed XAS spectrum by 20%, as in previous work.[29–31]

8. Modeling of Biased Interfaces using Continuum Models

In the modeling of biased interfaces using continuum models we assumed that in the thermodynamic equilibrium the ion concentration profiles account for the relaxation of electrostatic forces and that interconversion of ions is governed by equilibrium constants K_1 and K_2. The self-consistent solutions of the corresponding generalized Poisson-Boltzmann equation provided the complementary picture of speciation at biased Pt-electrode interfaces.

8.1 General formalism

To build the continuum model including three types of ions (sulfate, bisulfate, and hydronium), all of which have finite size and can specifically adsorb on the electrode surface except hydronium, we used a free energy functional that has the following form:[32]

$$
\Omega[\varphi(\vec{r}); \rho_{\pm}(r)]
$$

$$
= \int d\vec{r} \left\{ -\frac{\varepsilon(\vec{r})}{8\pi} |\nabla\varphi|^2 + e\varphi(\rho_+ - \rho_{1-} - \rho_{2-}) + \Phi_1(\vec{r})\rho_{1-} + \Phi_2(\vec{r})\rho_+ + \Phi_3(\vec{r})\rho_{2-} \right.
$$

$$
\left. - \mu_{1-}\rho_{1-} - \mu_{2-}\rho_{2-} - \mu_+\rho_+ \right\}
$$

$$
+ \frac{k_B T}{a^3} \int d\vec{r} \{ a^3\rho_{1-}\ln a^3\rho_{1-} + a^3\rho_{2-}\ln a^3\rho_{2-} + a^3\rho_+\ln a^3\rho_+
$$

$$
+ (1 - a^3\rho_{1-} - a^3\rho_{2-} - a^3\rho_+)\ln(1 - a^3\rho_{1-} - a^3\rho_{2-} - a^3\rho_+) \}.
$$

The Poisson-Boltzmann equation, as well as concentration profiles for ions, were obtained via the variational method:

$$
\nabla(\varepsilon(\vec{r})\nabla\varphi) = -4\pi e\left(\rho_+ - \rho_{1-} - 2\rho_{2-}\right)
$$

with boundary conditions $\frac{\partial\varphi}{\partial z}|_{z\to\infty} = 0$, $\frac{\partial\varphi}{\partial z}|_{z\to 0} = -\frac{\sigma}{\varepsilon_0\varepsilon}$, where σ is the surface charge density.

8.2 Input parameters

In this approximation the size of all ions was set equally to 6Å. Such simplification would slightly underestimate the concentration of hydronium ions because their actual size is smaller than that of (bi)sulfate ions. The overall surface coverage by ions would be overestimated since we did not consider the solvent (water) molecules explicitly.

To reflect the inhomogeneity in dielectric response of water near the surface, we used a spatially dependent dielectric function that has the following form:

$$
\varepsilon(z) = 1 + \frac{\varepsilon - 1}{1 + exp\left(-\alpha(z - z_0')\right)},
$$

where $\varepsilon = 78.3$, $\alpha = 4\ \text{Å}^{-1}$, and $z_0' = 2.8\ \text{Å}$.

The adsorption potentials $\Phi_{1,2,3}(\vec{r})$ were adapted from the FPMD free energy calculations (Fig. S9a) and then renormalized by Coulombic potentials of the image charge interaction (the interaction of a point charge with an ideal metal surface in the media with inhomogeneous dielectric function $\varepsilon(z)$ as defined earlier), as the first term in the Green's function of equation $\nabla(\varepsilon(z)\nabla\varphi) = -4\pi\delta(r - \vec{r}')$. The normalization terms generally have the following forms:

$$U(z)[eV] = -\frac{3.6\ \alpha^2}{\varepsilon(z)z[\text{Å}]},$$

where α is the charge on the ion.

The resulting potentials were then approximated with Morse potentials:

$$\Phi(z) = E_{ads}\left(1 - e^{-k(z - z_0)}\right)^2 - E_{ads}.$$

The adsorption energy E_{ads} is 0.12 eV for sulfate ions and 0.14 eV for bisulfate, which reflects the higher penalty for de-solvation of a divalent ion (11.3 eV) as compared to a monovalent ion (3.2 eV).[33] The slope parameter k was set to 4 and $z_0 = 2.7\text{Å}$. For hydronium ions we assume no specific adsorption by imposing a repulsive wall at $z = 2.2\text{Å}$.

We used the equilibrium constants reported in the literature[34] (K_1=1000, K_2=0.0102) to calculate the bulk equilibrium concentrations of ions. In a 0.05M H_2SO_4 solution, the equilibrium concentrations of sulfate, bisulfate, and hydronium ions are calculated to be 0.0075, 0.042, and 0.057M, respectively. Based on the thermodynamic cycle illustrated in Fig. S10, the equilibrium constant for adsorbed (bi)sulfate ions needs to be modified as follows:

$$K_2' = K_2 \frac{K_{ads}^{SO_4^{2-}}}{K_{ads}^{HSO_4^-}}.$$

Based on our FPMD simulations, the adsorption free energy of sulfate and bisulfate ions are almost equal (Fig. S9a) and therefore $K_2' \approx K_2$.

8.3 Self-consistent solutions

We used the scheme illustrated in Fig. S11 to obtain the equilibrium distribution of ions near the electrified surface. The results are shown in Fig. S12 where we compare the profiles with and without an additional equilibration based on the equilibrium constants K_1, K_2'. As one can see, at sufficiently positive potentials sulfate ions dominate in the interfacial region.

We also obtained the surface excess of ions as a function of surface charge density (Fig. S13a), and electrode potential (Fig. S13b), by integrating the ion concentration profiles over the interfacial regions at a given surface charge density or electrode potential. The results shown in Fig. S13 clearly indicated that co-adsorption of bisulfate and sulfate ions dominates in the interfacial region at potentials above 0.1V. The asymmetry of the curves arises from the differences in adsorption potentials and the charges between hydronium and (bi)sulfate ions.

Supporting Figures
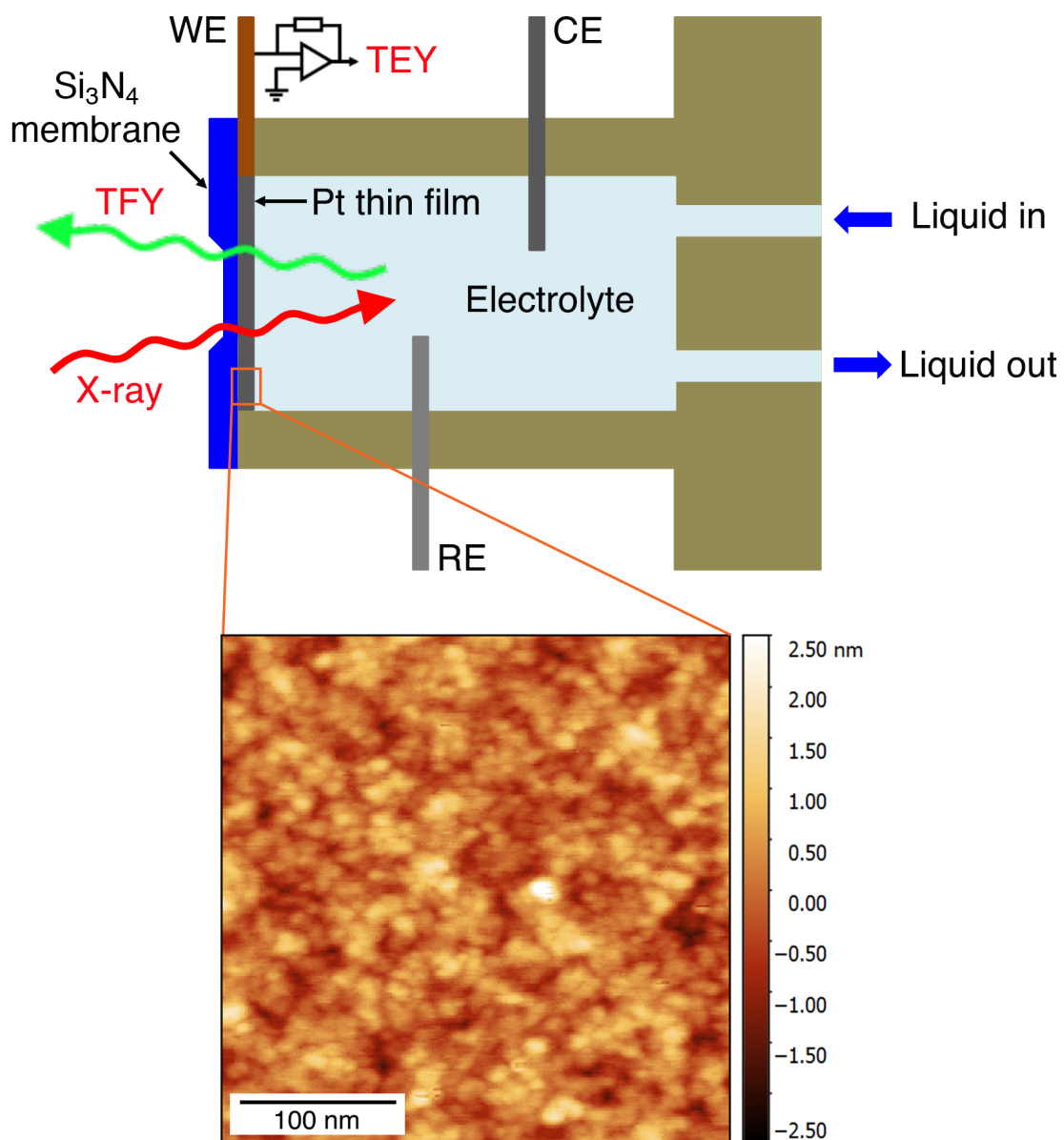
Figure S1. Schematics of the flow liquid cell and typical topological AFM Image of the evaporated Pt thin film (RMS roughness ~ 0.5nm).
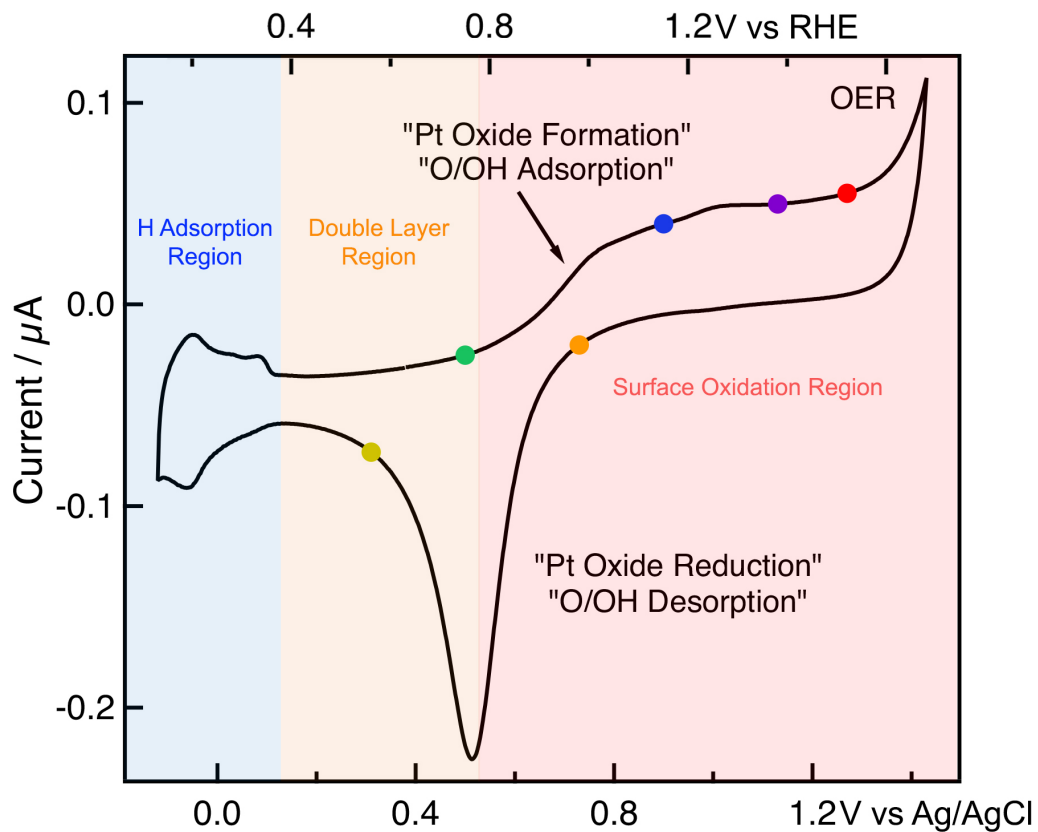
Figure S2. Typical CV curve of the thin film Pt electrode in 0.05M H_2SO_4 solution measured in the liquid cell with Pt CE and Ag/AgCl RE. The scan rate is 50mV/s. The curve was divided into three regions, each colored and labeled based on conventional models in the electrochemical literature. The potential scale with respect to RHE (assuming pH = 1) is shown at the top of the graph for reference.
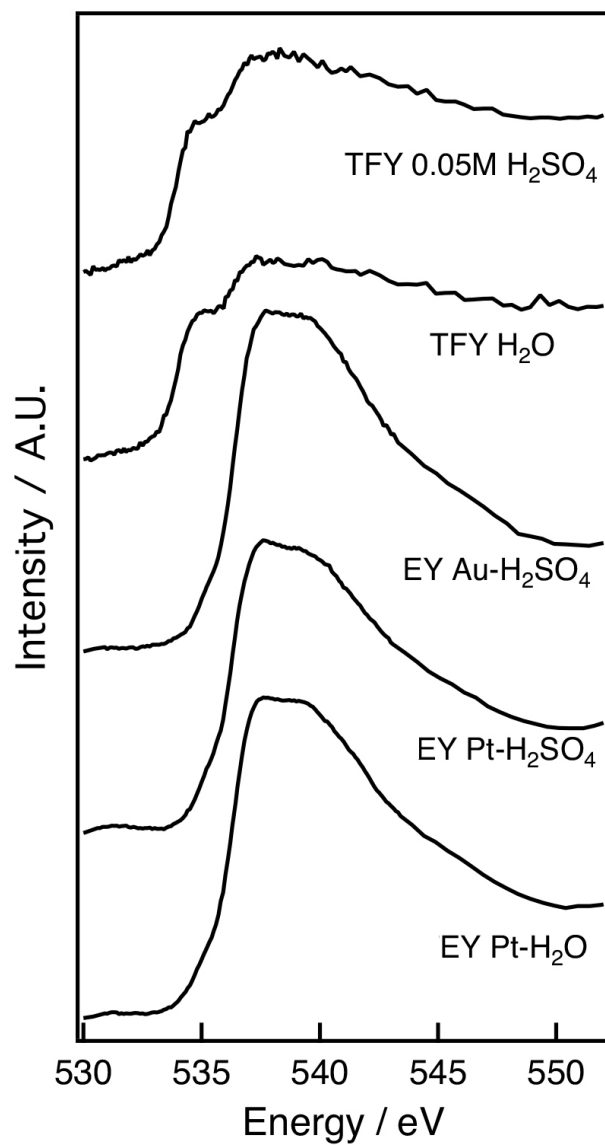
Figure S3. Comparison of O K-edge EY-XAS spectra under OCP at Au-H₂SO₄(aq), Pt-H₂SO₄(aq), Pt-H₂O interfaces and TFY-XAS spectra of pure H₂O and 0.05M H₂SO₄ solution.
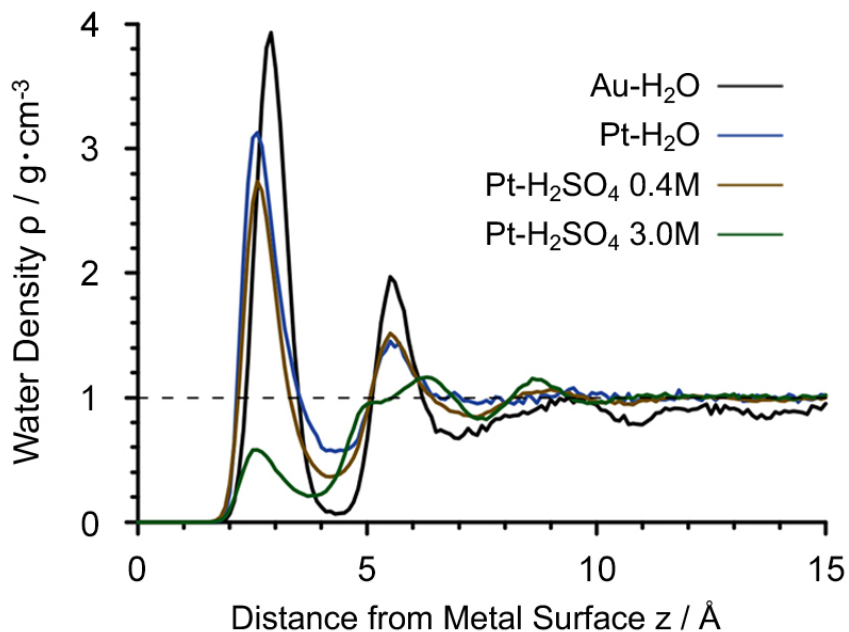
Figure S4: Water mass density distribution at various interfaces from FPMD simulations. The center of mass position of each water molecule is discretized in 0.1Å bins and averaged every 10fs over the last 10ps of the FPMD trajectory. Each distribution profile shows three structured water layers: the first molecular layer lies within 1.2-3.9Å with a peak maximum at ~3Å, the second interfacial layer lies at 3.9-6.6 Å from the surface, and a possible third layer at 6.6-9.4Å, after which the density converges to the bulk value.
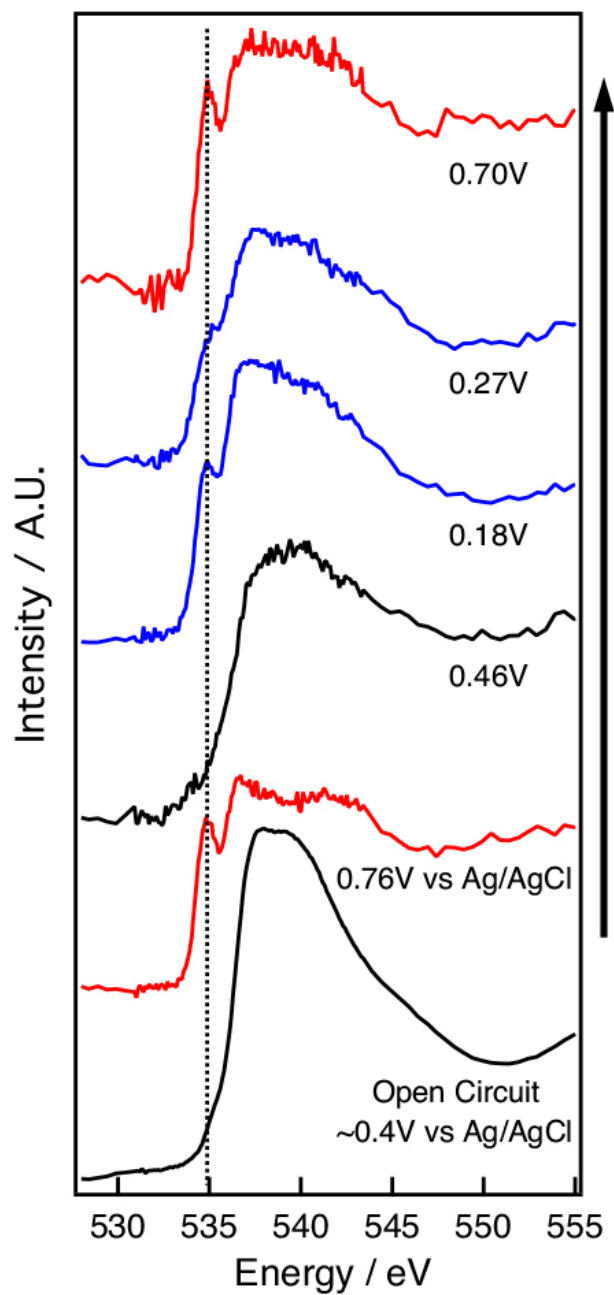
Figure S5. *Operando* O K-edge EY-XAS spectra of the Au-H_2SO_4(aq) interface at different potentials. The black arrow indicates the order of spectra acquisition.
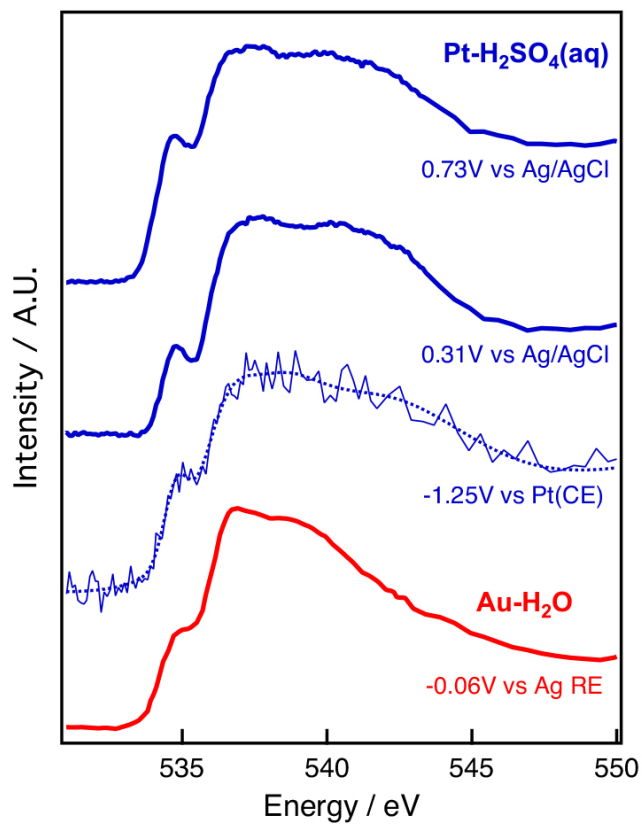
Figure S6. Comparison of O K-edge EY-XAS spectra collected at Pt-H_2SO_4(aq) interface at 0.73V and 0.31V vs Ag/AgCl and at -1.25V vs Pt CE, as well as EY-XAS spectrum at Au-H_2O interface at -0.06V vs Ag pseudo-reference electrode as previously reported.[1]
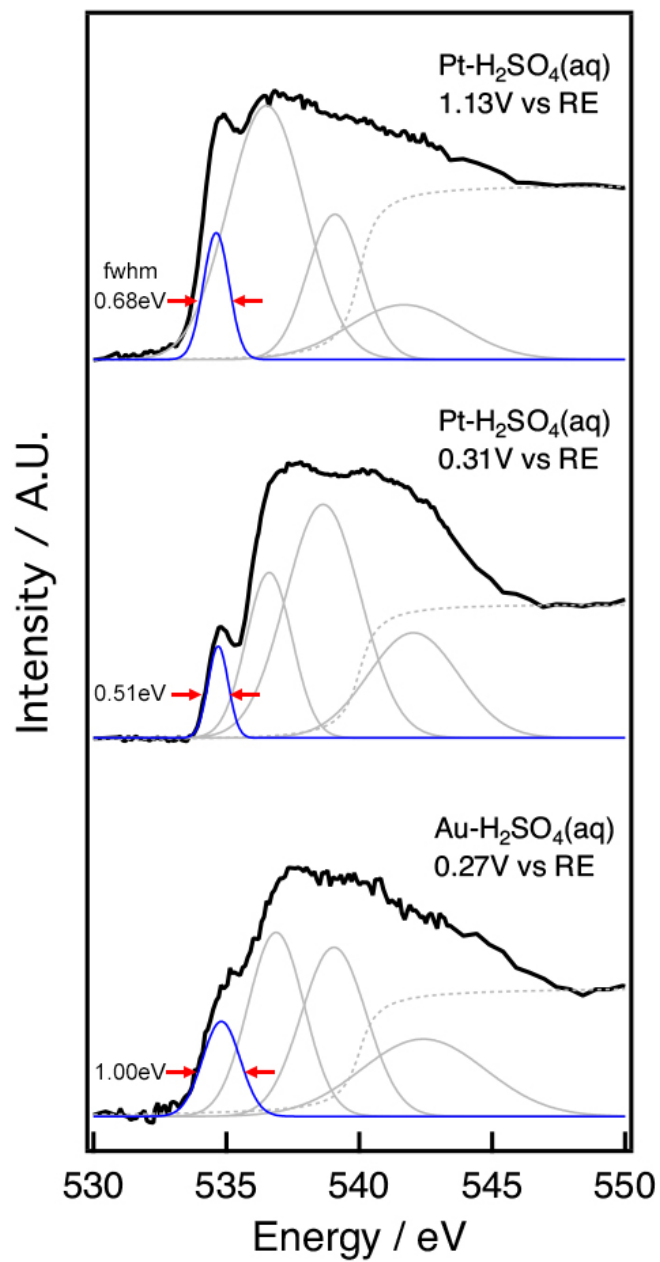
Figure S7. Peak deconvolution of EY-XAS spectra of the Pt-H_2SO_4(aq) interface at 1.13V and 0.31V vs Ag/AgCl (above OCP) and of Au/H_2SO_4(aq) interface at 0.27V vs Ag/AgCl (below OCP).
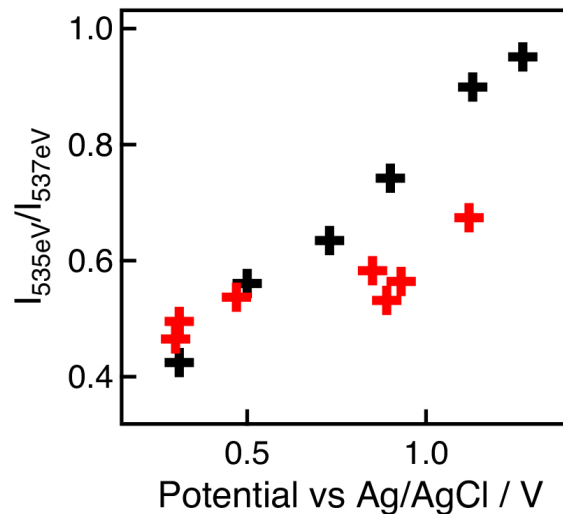
Figure S8. Dependence of pre-peak to main-peak ratios (I_{535eV}/I_{537eV}) in the O K-edge EY-XAS of Pt-H_2SO_4(aq) interface from two sets of experiments. The difference in the slope is possibly due to the change of chemical states of Pt CE during long period experiments at a fixed potential during each spectrum.
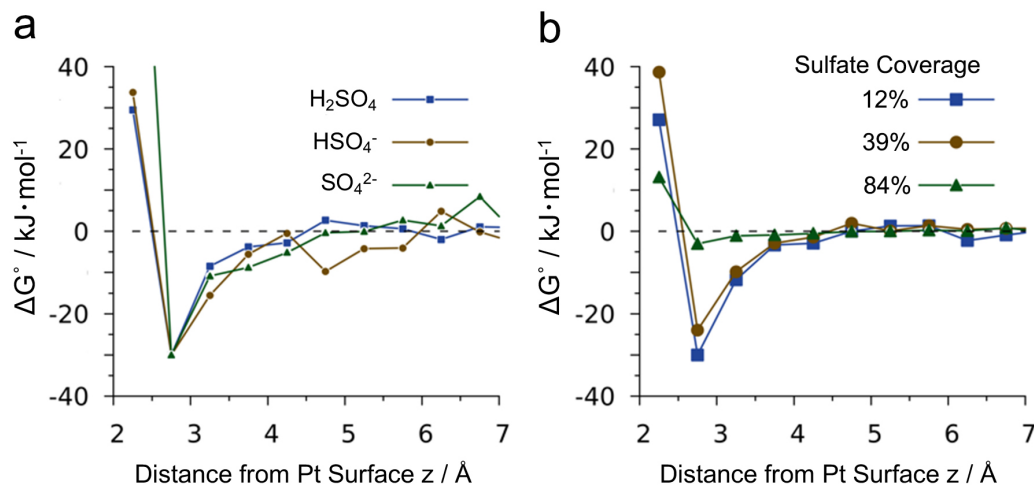

Figure S9. Calculated binding free energy profile of sulfate species at the Pt-H_2SO_4(aq) interface. **(a)** Comparison of profiles of isolated H_2SO_4 (blue squares), HSO_4^- (brown circles) and SO_4^{2-} (green triangles) molecules. **(b)** SO_4^{2-} binding free energy profile at three surface coverages, corresponding to bulk concentration 0.4M, 1.0M, and 3.0M, respectively.
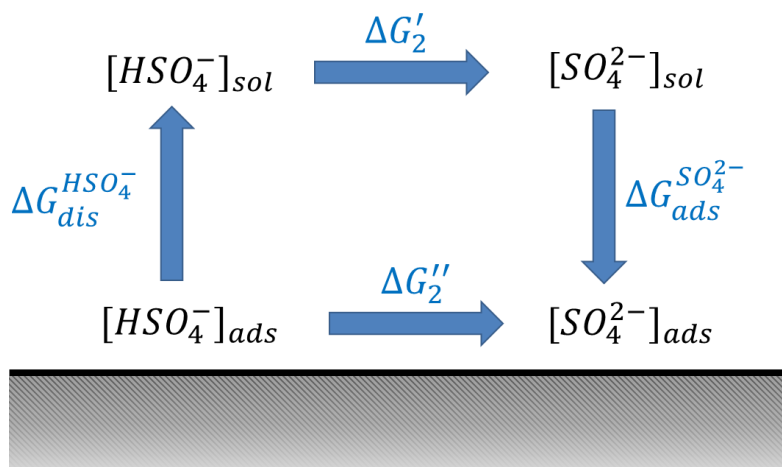
Figure S10. Thermodynamic cycle for evaluation of the equilibrium constant of adsorbed bisulfate ions.
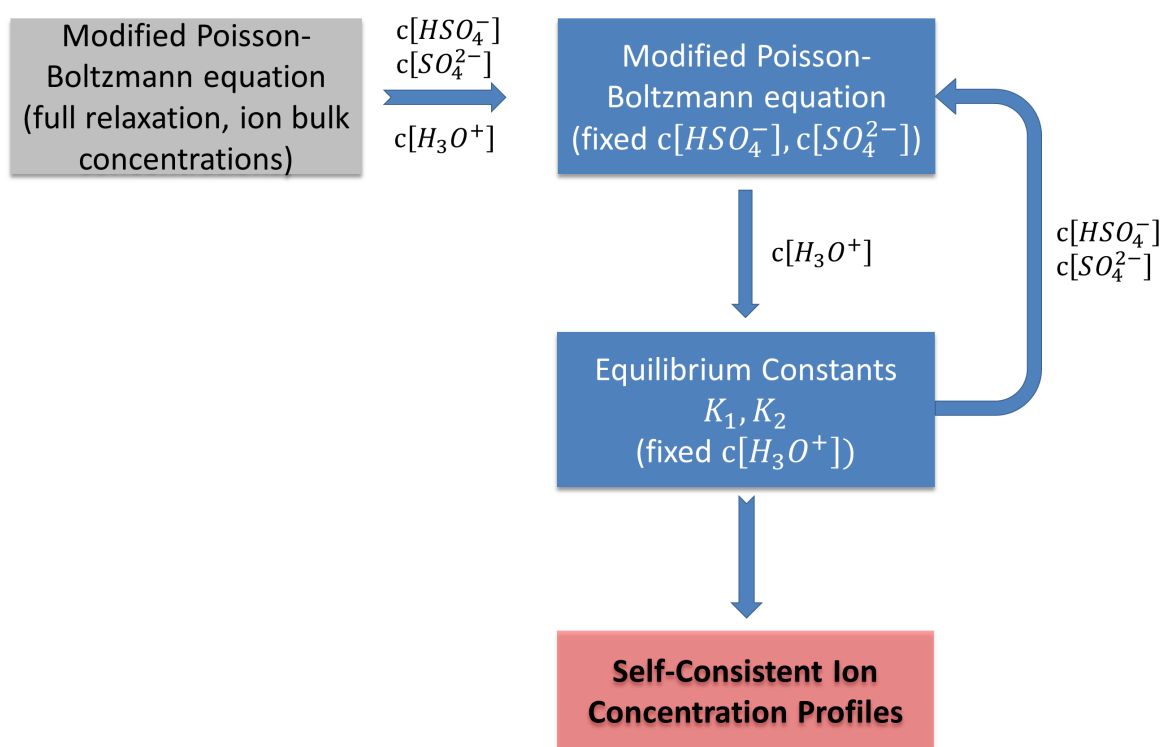

Figure S11. Scheme of the calculation flow towards a self-consistent solution of the modified Poisson-Boltzmann equation with external constraints associated with inter-conversion of sulfate and bisulfate ions.
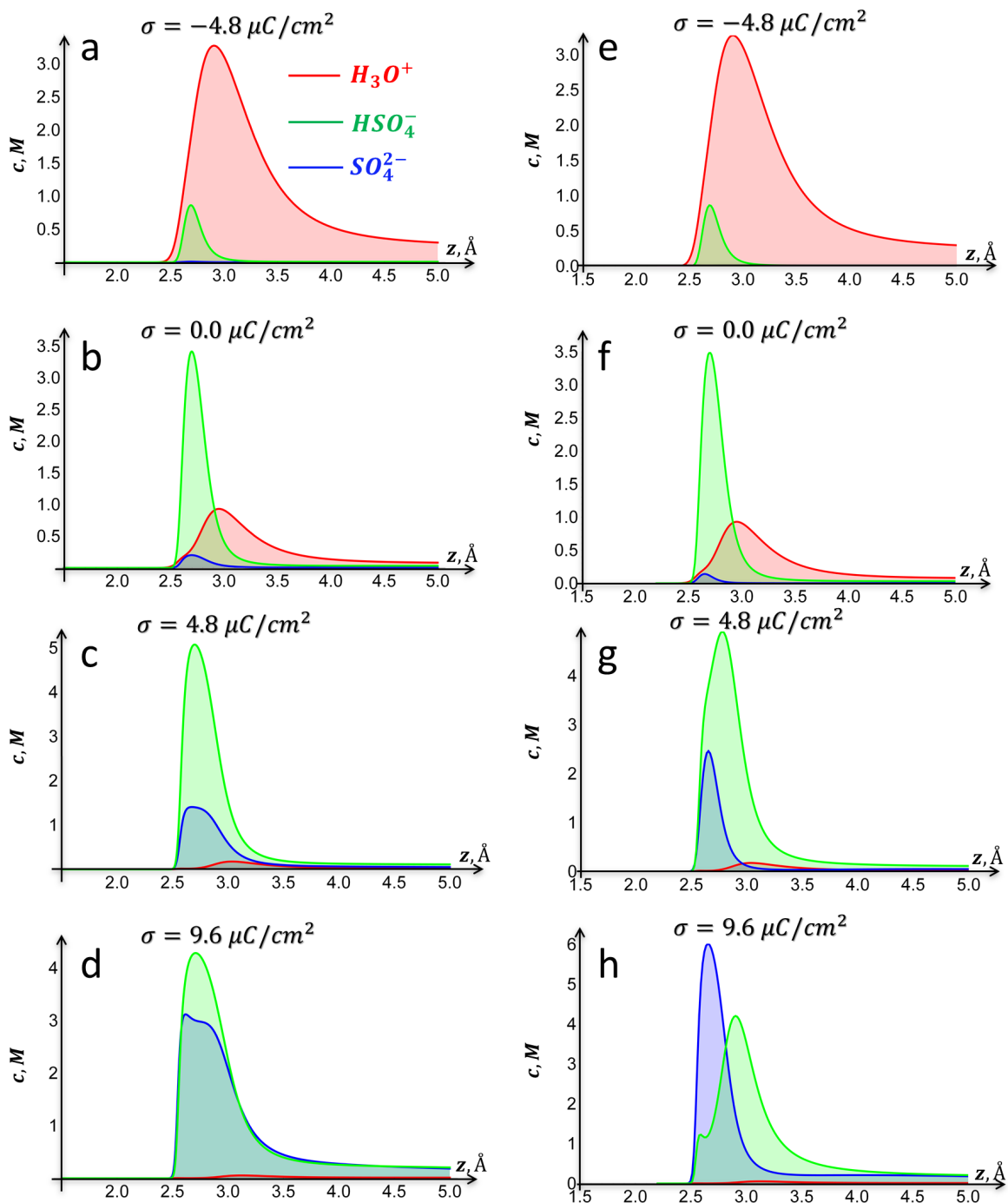
Figure S12. Ion concentration profiles calculated using continuum model without (**a-d**) and with (**e-h**) equilibration of concentrations due to the ion inter-conversion at various surface charge densities.
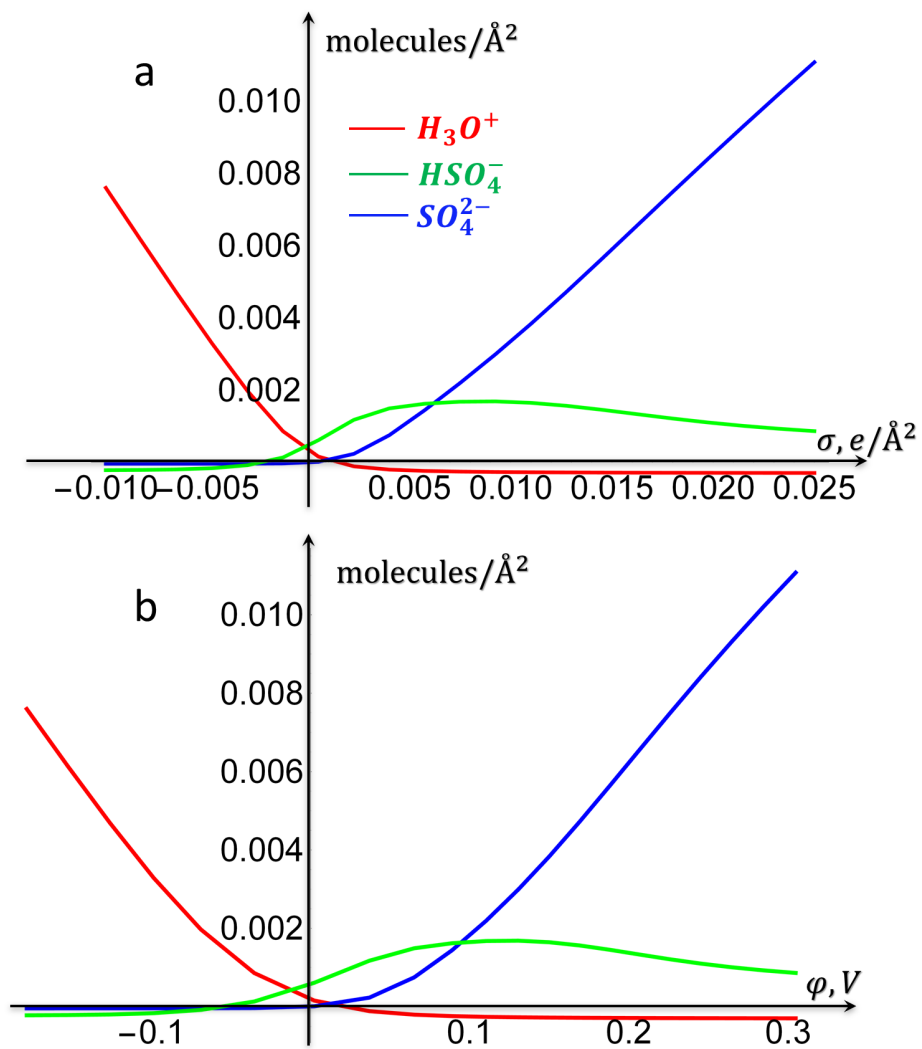
Figure S13. The profiles of surface excess of ions as a function of surface charge density (**a**) and as a function of the electrode potential (**b**). Potentials are referenced to the value in the bulk electrolyte. Negative values on the y axis correspond to deficiency while positive values indicate excess.
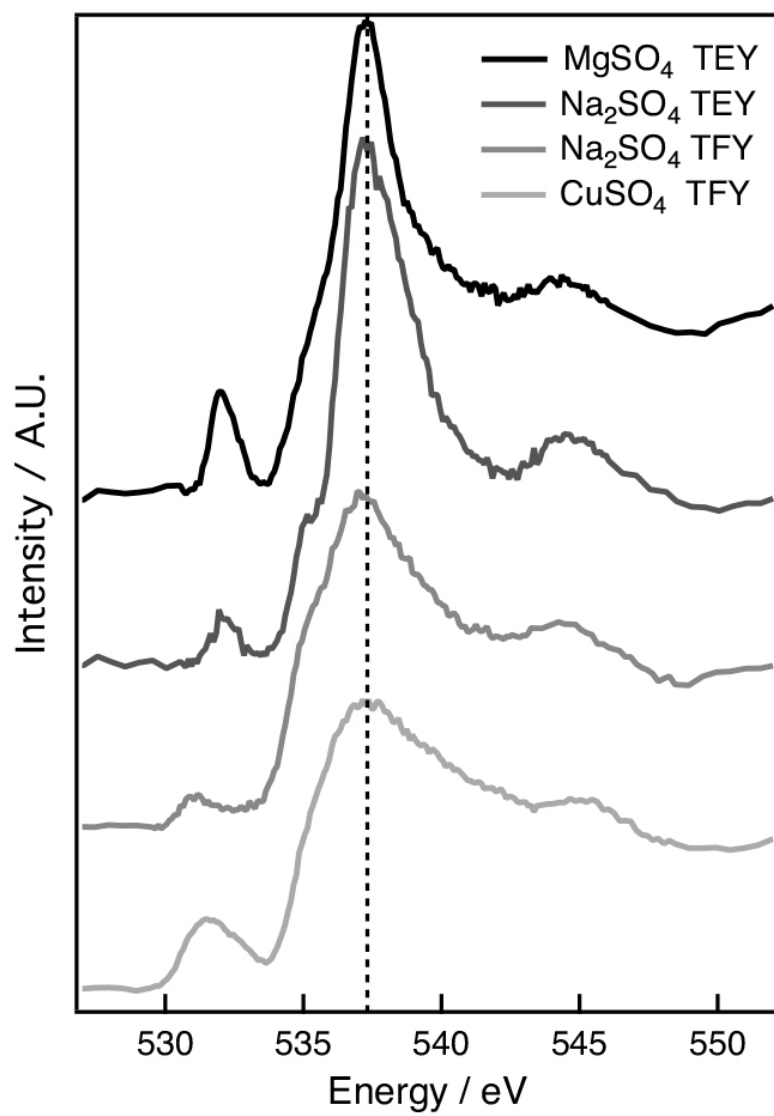
Figure S14. O K-edge XAS spectra of the salt crystals of various sulfates.
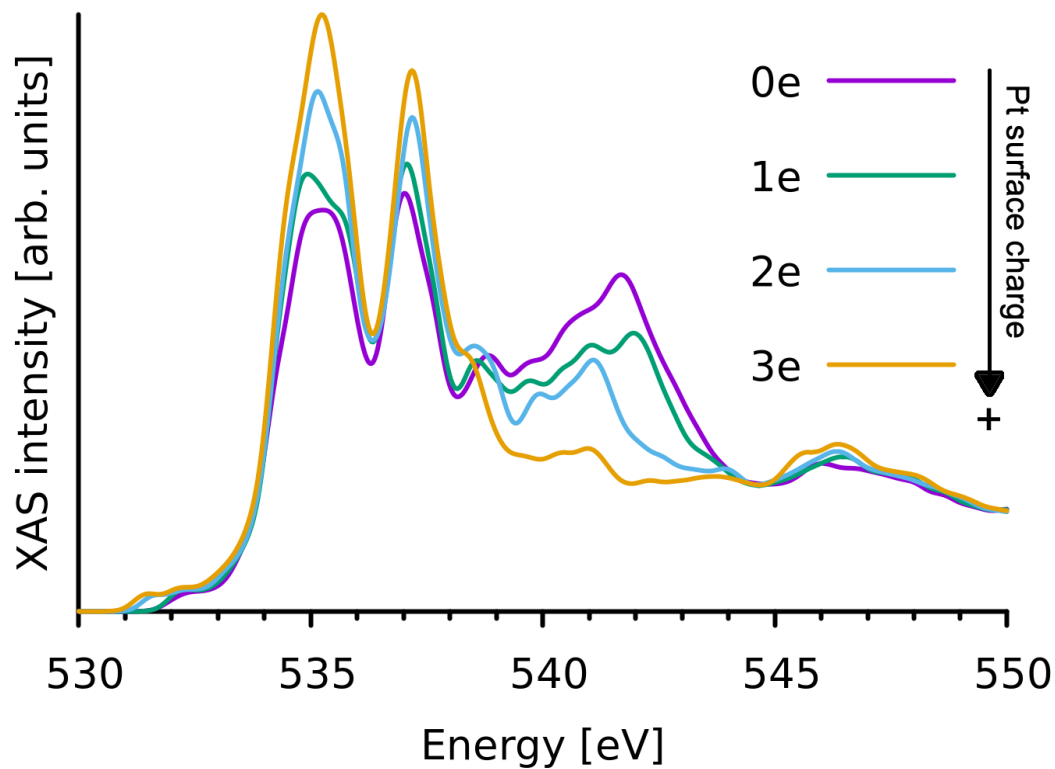
Figure S15. Simulated O K-edge XAS of sulfate (SO_4^{2-}) anions at the Pt-H_2SO_4(aq) interface with different surface charge. Each simulation cell of the size 11.2×9.7×53.4 Å^3 containing two sulfate anions and four (purple), three (green), two (blue) and one (brown) hydronium (H_3O^+) cations. Each cell underwent NVT FPMD for 2ps and the resulting spectrum is the numerical average of 20 individual snapshots from the last 1ps FPMD (evenly separated by 50fs).

References

(1)   Velasco-Velez, J. J.; Wu, C. H.; Pascal, T. A.; Wan, L. F.; Guo, J.; Prendergast, D.; Salmeron, M. The Structure of Interfacial Water on Gold Electrodes Studied by X-Ray Absorption Spectroscopy. *Science* **2014**, *346*, 831–834.

(2)   Nilsson, A.; Nordlund, D.; Waluyo, I.; Huang, N.; Ogasawara, H.; Kaya, S.; Bergmann, U.; Näslund, L.-Å.; Öström, H.; Wernet, P.; et al. X-Ray Absorption Spectroscopy and X-Ray Raman Scattering of Water and Ice; an Experimental View. *J. Electron Spectros. Relat. Phenomena* **2010**, *177* (2–3), 99–129.

(3)   Lippert, G.; Hutter, J.; Parrinello, M. A Hybrid Gaussian and Plane Wave Density Functional Scheme. *Mol. Phys.* **1997**, *92* (3), 477–488.

(4)   VandeVondele, J.; Krack, M.; Mohamed, F.; Parrinello, M.; Chassaing, T.; Hutter, J. Quickstep: Fast and Accurate Density Functional Calculations Using a Mixed Gaussian and Plane Waves Approach. *Comput. Phys. Commun.* **2005**, *167* (2), 103–128.

(5)   VandeVondele, J.; Hutter, J. Gaussian Basis Sets for Accurate Calculations on Molecular Systems in Gas and Condensed Phases. *J. Chem. Phys.* **2007**, *127* (11), 114105.

(6)   Perdew, J. P.; Burke, K.; Ernzerhof, M. Generalized Gradient Approximation Made Simple. *Phys. Rev. Lett.* **1996**, *77* (18), 3865–3868.

(7)   Goedecker, S.; Teter, M.; Hutter, J. Separable Dual-Space Gaussian Pseudopotentials. *Phys. Rev. B* **1996**, *54* (3), 1703–1710.

(8)   Krack, M. Pseudopotentials for H to Kr Optimized for Gradient-Corrected Exchange-Correlation Functionals. *Theor. Chem. Acc.* **2005**, *114* (1–3), 145–152.

(9)   Genovese, L.; Deutsch, T.; Goedecker, S. Efficient and Accurate Three-Dimensional Poisson Solver for Surface Problems. *J. Chem. Phys.* **2007**, *127* (5), 054704.

(10)   Grimme, S.; Antony, J.; Ehrlich, S.; Krieg, H. A Consistent and Accurate Ab Initio Parametrization of Density Functional Dispersion Correction (DFT-D) for the 94 Elements H-Pu. *J. Chem. Phys.* **2010**, *132* (15), 154104.

(11)   Wan, Q.; Spanu, L.; Gygi, F.; Galli, G. Electronic Structure of Aqueous Sulfuric Acid from First-Principles Simulations with Hybrid Functionals. *J. Phys. Chem. Lett.* **2014**, *5* (15), 2562–2567.

(12)   Torrie, G. M.; Valleau, J. P. Nonphysical Sampling Distributions in Monte Carlo Free-Energy Estimation: Umbrella Sampling. *J. Comput. Phys.* **1977**, *23*, 187–199.

(13)   Grossfield, A. WHAM: An Implementation of the Weighted Histogram Analysis Method, Version 2.0.7. Rochester University: Rochester, NY 2013.

(14)   Chodera, J. D.; Swope, W. C.; Pitera, J. W.; Seok, C.; Dill, K. A. Use of the Weighted Histogram Analysis Method for the Analysis of Simulated and Parallel Tempering Simulations. *J. Chem. Theory Comput.* **2007**, *3* (1), 26–41.

(15)   Pascal, T. A.; Boesenberg, U.; Kostecki, R.; Richardson, T. J.; Weng, T.-C.; Sokaras, D.; Nordlund, D.; McDermott, E.; Moewes, A.; Cabana, J.; et al. Finite Temperature Effects on the X-Ray Absorption Spectra of Lithium Compounds: First-Principles Interpretation of X-Ray Raman Measurements. *J. Chem. Phys.* **2014**, *140* (3), 034107.

(16)   England, A. H.; Duffin, A. M.; Schwartz, C. P.; Uejio, J. S.; Prendergast, D.; Saykally, R. J. On the Hydration and Hydrolysis of Carbon Dioxide. *Chem. Phys. Lett.* **2011**, *514* (4–6), 187–195.

(17)   Prendergast, D.; Galli, G. X-Ray Absorption Spectra of Water from First Principles Calculations. *Phys. Rev. Lett.* **2006**, *96* (21), 215502.

(18)   Vanderbilt, D. Soft Self-Consistent Pseudopotentials in a Generalized Eigenvalue Formalism. *Phys. Rev. B* **1990**, *41* (11), 7892–7895.

(19)   Giannozzi, P.; Baroni, S.; Bonini, N.; Calandra, M.; Car, R.; Cavazzoni, C.; Ceresoli, D.; Chiarotti, G. L.; Cococcioni, M.; Dabo, I.; et al. QUANTUM ESPRESSO: A Modular and Open-Source Software Project for Quantum Simulations of Materials. *J. Phys. Condens. Matter* **2009**, *21* (39), 395502.

(20)   Shirley, E. Optimal Basis Sets for Detailed Brillouin-Zone Intergrations. *Phys. Rev. B* **1996**, *54* (23), 464–469.

(21)   Prendergast, D.; Louie, S. G. Bloch-State-Based Interpolation: An Efficient Generalization of the Shirley Approach to Interpolating Electronic Structure. *Phys. Rev. B* **2009**, *80* (23), 235126.

(22)   Taillefumier, M.; Cabaret, D.; Flank, A.-M. A.; Mauri, F. X-Ray Absorption Near-Edge Structure Calculations with Pseudopotentials. Application to K-Edge in Diamond and α-Quartz. *Phys. Rev. B* **2002**, *66* (66), 1–11.

(23)   Jiang, P.; Prendergast, D.; Borondics, F.; Porsgaard, S.; Giovanetti, L.; Pach, E.; Newberg, J.; Bluhm, H.; Besenbacher, F.; Salmeron, M. Experimental and Theoretical Investigation of the Electronic Structure of Cu_2O and CuO Thin Films on Cu(110) Using x-Ray Photoelectron and Absorption Spectroscopy. *J. Chem. Phys.* **2013**, *138* (2), 024704.

(24)   Sham, T. K.; Yang, B. X.; Kirz, J.; Tse, J. S. K-Edge near-Edge x-Ray-Absorption Fine Structure of Oxygen- and Carbon-Containing Molecules in the Gas Phase. *Phys. Rev. A* **1989**, *40* (2), 652–669.

(25)   Cohen, A. J.; Mori-Sánchez, P.; Yang, W. Fractional Charge Perspective on the Band Gap in Density-Functional Theory. *Phys. Rev. B* **2008**, *77* (11), 115123.

(26)   Mori-Sánchez, P.; Cohen, A. J.; Yang, W. Localization and Delocalization Errors in Density Functional Theory and Implications for Band-Gap Prediction. *Phys. Rev. Lett.* **2008**, *100* (14), 146401.

(27)   Fuchs, F.; Furthmüller, J.; Bechstedt, F.; Shishkin, M.; Kresse, G. Quasiparticle Band Structure Based on a Generalized Kohn-Sham Scheme. *Phys. Rev. B* **2007**, *76* (11), 115109.

(28)   Aulbur, W. G.; Jönsson, L.; Wilkins, J. W. Quasiparticle Calculations in Solids; 2000; pp 1–218. DOI: 10.1016/S0081-1947(08)60248-9

(29)   Pascal, T.; Wujcik, K.; Velasco-Velez, J.; Wu, C.; Teran, A.; Kapilashrami, M.; Cabana, J.; Guo, J.; Salmeron, M.; Balsara, N.; et al. The X-Ray Absorption Spectra of Dissolved Polysulfides in Lithium–Sulfur Batteries from First Principles. *J. Phys. Chem. Lett.* **2014**, *5*, 1547–1551.

(30)   Pascal, T. A.; Pemmaraju, C. D.; Prendergast, D. X-Ray Spectroscopy as a Probe for Lithium Polysulfide Radicals. *Phys. Chem. Chem. Phys.* **2015**, *17* (12), 7743–7753.

(31)   Pascal, T. A.; Villaluenga, I.; Wujcik, K. H.; Devaux, D.; Jiang, X.; Wang, D. R.; Balsara, N.; Prendergast, D. Liquid Sulfur Impregnation of Microporous Carbon Accelerated by Nanoscale Interfacial Effects. *Nano Lett.* **2017**, *17* (4), 2517–2523.

(32)   Baskin, A.; Prendergast, D. Improving Continuum Models to Define Practical Limits for Molecular

Models of Electrified Interfaces. *J. Electrochem. Soc.* **2017**, *164* (11), E3438–E3447.

(33)   Marcus, Y. Ionic Radii in Aqueous Solutions. *Chem. Rev.* **1988**, *88* (8), 1475–1498.

(34)   Dawson, B. S. W.; Irish, D. E.; Toogood, G. E. Vibrational Spectral Studies of Solutions at Elevated Temperatures and Pressures. 8. A Raman Spectral Study of Ammonium Hydrogen Sulfate Solutions and the Hydrogen Sulfate-Sulfate Equilibrium. *J. Phys. Chem.* **1986**, *90* (2), 334–341.